

This discussion paper is/has been under review for the journal *Atmospheric Chemistry and Physics (ACP)*. Please refer to the corresponding final paper in *ACP* if available.

Aerosol distribution around Svalbard

A. Dörnbrack et al.

Aerosol distribution around Svalbard during intense easterly winds

A. Dörnbrack¹, I. S. Stachlewska^{2,3}, C. Ritter³, and R. Neuber³

¹DLR Oberpfaffenhofen, Institut für Physik der Atmosphäre, 82230 Wessling, Germany

²Institute of Geophysics, Faculty of Physics, University of Warsaw, Pasteura 7, 02-093 Warsaw, Poland

³Alfred-Wegener Institut für Polar- und Meeresforschung (AWI), Forschungsstelle Potsdam, Telegraphenberg 43A, 14473 Potsdam, Germany

Received: 30 June 2009 – Accepted: 3 August 2009 – Published: 5 August 2009

Correspondence to: A. Dörnbrack (andreas.doernbrack@dlr.de)

Published by Copernicus Publications on behalf of the European Geosciences Union.

Title Page

Abstract

Introduction

Conclusions

References

Tables

Figures

◀

▶

◀

▶

Back

Close

Full Screen / Esc

Printer-friendly Version

Interactive Discussion



Abstract

This paper reports on backscatter and depolarization measurements by an airborne lidar in the Arctic during the ASTAR 2004 campaign. A unique weather situation facilitated the observation of the aerosol concentration under strongly forced atmospheric conditions. The vigorous easterly winds distorted the flow past Svalbard in such a way that unique mesoscale features were visible in the remote-sensing observations. Mesoscale numerical modelling was applied to identify the sources of the aerosol plumes and to explain the observed patterns.

1 Introduction

In the Arctic, properties of tropospheric aerosol particles have been measured in numerous field studies beginning in the 1970s (Radke et al., 1984; Schnell, 1984; Schnell et al., 1989; Thomason et al. 2003; Treffeisen et al., 2004; Yamanouchi et al., 2005). Knowledge of the spatial and seasonal distribution of aerosol particles is needed to estimate the induced changes in the Earth radiative budget via direct (e.g. Schwartz and Andrea, 1996; Rinke et al., 2004; Ritter et al., 2005) and indirect (e.g. Garrett et al., 2002; Lubin and Vogelmann, 2006) effects on the solar (0.3–5 μm) and thermal-infrared (5–50 μm) radiation. In many instances, the interpretation of observed aerosol particle distributions, especially in the vicinity of complex topography or near the ice edge, requires to know the meso- and microscale atmospheric state. However, this knowledge might not be sufficient as the additionally needed aerosol particle sources and their composition are often not well characterized.

We report about airborne aerosol backscatter observations made in the vicinity of Svalbard during the ASTAR 2004¹ field campaign. During ASTAR 2004 an airborne

¹ASTAR 2004 – Arctic Study of Tropospheric Aerosol, Clouds and Radiation – was organized by the Alfred-Wegener Institut für Polar- und Meeresforschung Bremerhaven; see <http://www.awi.de>.

Aerosol distribution around Svalbard

A. Dörnbrack et al.

Title Page

Abstract

Introduction

Conclusions

References

Tables

Figures

◀

▶

◀

▶

Back

Close

Full Screen / Esc

Printer-friendly Version

Interactive Discussion



**Aerosol distribution
around Svalbard**

A. Dörnbrack et al.

[Title Page](#)[Abstract](#)[Introduction](#)[Conclusions](#)[References](#)[Tables](#)[Figures](#)[◀](#)[▶](#)[◀](#)[▶](#)[Back](#)[Close](#)[Full Screen / Esc](#)[Printer-friendly Version](#)[Interactive Discussion](#)

lidar was employed to investigate the Arctic aerosol distribution in the lowermost troposphere around Svalbard. In the period from 18–21 May 2004, the meteorological situation facilitated observations under nearly stationary but strong wind conditions. A slowly moving cyclone between northern Scandinavia and Svalbard and a stationary anticyclone north of 80° N caused a strong easterly flow across the islands. This favorable situation allowed airborne observations of the aerosol distribution under strongly forced meteorological conditions in the fjord system and in the lee of Svalbard.

The background aerosol load was exceptionally low at the time of the observations. As reported by Engvall et al. (2008), the ASTAR 2004 campaign encountered “even less contaminated conditions than usual at this time of the year”. Therefore, the question arises if the observed aerosol particles resulted mainly from emissions of local sources. The distinct mesoscale pattern of the observed aerosol backscatter ratio at the different measurement locations support this hypothesis.

One goal of this paper is to explain these different mesoscale aerosol patterns of the airborne lidar observations. For this purpose, operational meteorological analyses of the European Centre of Medium Range Weather Forecast (ECMWF) and high-resolution numerical simulations are applied. In particular, the geophysical fluid solver EULAG (Prusa et al., 2008) has been expanded by three transport equations for scalar quantities representing different sources of aerosol particles. On the other hand, the observed aerosol distributions are utilized to study the characteristics of the stable atmospheric flow over Svalbard. In this sense, the aerosols mobilized from local sources might serve as a means of flow visualisation.

Previous numerical simulations of the mesoscale flow around Svalbard concentrated on the impact on the local weather forecast, especially on ship routing. For example, Sandvik and Furevik (2002) highlighted the enormous effect Svalbards topography plays in modifying the local wind field in the valleys and coastal areas surrounding the islands. These authors reported downstream coastal jets with maximum velocities up to 3 times the value of the upstream flow. Furthermore, and in accordance with our findings, they argued that these local wind systems influence the high-latitude air-

sea interaction processes in a significant way by increasing the surface fluxes of heat and constituents in a similar manner as it is observed over the Irminger Sea east of Greenland (Pickart et al., 2003).

The remaining parts of the paper are arranged as follows: the next section presents the airborne lidar observations and characterizes the aerosol particles by showing graphs of backscatter ratio and depolarization. Section 3 presents the mesoscale numerical simulations. Section 4 discusses the results of the present study to what extent meteorological factors explain the observed distribution of aerosol particles.

2 Airborne lidar observations

The airborne aerosol backscatter observations analysed in this paper were obtained with the Airborne Mobile Aerosol Lidar AMALi (for the instrument specification, see Appendix A) onboard the AWI-POLAR 2 research aircraft² during the ASTAR 2004 campaign (17 May–10 June 2004). Data analysed here were collected under nearly clear-sky conditions in the Adventsdalen, the Isfjorden, and in the coastal areas west of Svalbard in the period from 18 till 21 May 2004.

2.1 Meteorological conditions

Figure 1 illustrates the meteorological situation in terms of temperature, geopotential height and wind speed at the 925 hPa pressure surface on the three measurement days. The maps are based on operational analyses of the European Centre of Medium Range Weather Forecast (ECMWF) with a spectral resolution of T_L 511 and 60 vertical hybrid σ – p levels. On 18 and 19 May 2004, prevailing cold easterly winds with $T < 263$ K at 925 hPa past Svalbard. In response to this flow, descending air formed a warm pool

²The AWI research aircraft POLAR 2 and 4 were the primary platforms for the ASTAR 2004 experiment. The aircraft were operating from Longyearbyen airport on Svalbard from 10 May 2004 until 18 June 2004; for more detailed information visit <http://www.awi.de>.

Aerosol distribution around Svalbard

A. Dörnbrack et al.

Title Page

Abstract

Introduction

Conclusions

References

Tables

Figures

◀

▶

◀

▶

Back

Close

Full Screen / Esc

Printer-friendly Version

Interactive Discussion



**Aerosol distribution
around Svalbard**

A. Dörnbrack et al.

($T \approx 267$ K at 925 hPa on 19 May 2004) in the wake region west of Prins Karls Foreland. Additionally and most remarkably, the flow around the islands resulted in a detached low-level jet with a horizontal wind speed of $V_H > 15 \text{ m s}^{-1}$ emanating from the northern tip of Svalbard, a phenomenon similar to Greenland's tip jet (e.g. Doyle and Shapiro, 1999; Orr et al., 2005).

The Moderate-Resolution Imaging Spectroradiometer (MODIS) satellite imagery (Fig. 2) illustrates the meteorological analyses by a snapshot from 19 May 2004 at 12:05 UTC. West of Svalbard, a cloud-free "Foehn" gap extended about half of the width of archipelago downstream. There, the brightness temperature difference to the upstream value amounts to $\Delta LST \approx 7$ K, where LST is the land-surface temperature (Fig. 2c). The white and peach-colored structures indicate cloud systems at different altitudes (Fig. 2b): Low-level clouds existed all around the islands. Especially, they appeared as rather compact and nearly east-west oriented bands over the pack-ice north of Svalbard. Upper-level cirrus mark the warm sector of the low over the Barents Sea that propagated slowly north-eastward. Associated with the low-level jet north of Svalbard, a nearly cloud-free wake extended several hundred kilometer downstream (cf. also NOAA AVHRR on 19 May 2004 at 14:41 UTC at <http://www.sat.dundee.ac.uk>).

On 19 May 2004, the horizontal wind speed V_H upstream of the northern parts of Svalbard varied between 8 and 13 m s^{-1} in the lower troposphere and there was no significant directional shear across the boundary layer. Given an upstream mean buoyancy frequency of $N = 0.01 \text{ s}^{-1}$ and a $V_H \approx 10 \text{ m s}^{-1}$ results in an inverse Froude number $\mathcal{F}^{-1} = N h_0 / V_H \approx 0.5 \dots 1.6$ for typical maximum elevations of the orography h_0 between 500 and 1600 m. Another dimensionless number describing the flow regime is the Rossby number $\mathcal{R} = V_H / L f$, where L is the mountain width and f the Coriolis parameter. Taking a typical mountain width L of 50...100 km, this results in Rossby numbers between 0.7 and 1.4. In a regime diagram (see Schär, 2002), the resulting flow is partially around and over Svalbard. Furthermore, for $\mathcal{R} \mathcal{F}^{-1} \geq 0.5$, balanced solutions (e.g. based on geostrophy or quasi-geostrophy) break down due to the splitting of the incident low-level flow upstream (Pierrehumbert, 1985). This justifies the usage

[Title Page](#)[Abstract](#)[Introduction](#)[Conclusions](#)[References](#)[Tables](#)[Figures](#)[◀](#)[▶](#)[◀](#)[▶](#)[Back](#)[Close](#)[Full Screen / Esc](#)[Printer-friendly Version](#)[Interactive Discussion](#)

of non-hydrostatic numerical simulations later on in this paper.

At the end of the observational period, the warm front of the approaching trough resulted in weaker winds from south-east. In the meteorological analyses for 21 May 2004, the low-level jet north of Svalbard still existed, however, with a magnitude of about 7 to 9 m s^{-1} it was significantly weaker. The warm pool and the wake shifted slightly northwards due to the southerly wind component. As the upstream sea-surface temperature remained nearly constant during the period, the associated warm air advection (upstream temperature increased by about 9 K at 925 K during the three days) enhanced the thermal stratification dramatically in the marine boundary layer, cf. the compression of isentropes in the vertical cross sections along the flight tracks as shown in Fig. 6a and b.

2.2 Lidar observations of 18 May 2004

The preconditions of the three research flights differed markedly: Whereas the patterns of the both flights on 19 and 21 May 2004 were designed after a meticulous meteorological planning to map the aerosol distribution downstream of Svalbard, the very first flight on 18 May 2004 was performed rather spontaneously after the unexpected occurrence of a dust storm in the Adventdalen. On 18 May 2004, significant loads of mineral dust were mobilized by the strong winds blowing through the snow-free Adventdalen. With the prevailing easterly winds, these particles were transported along the valley toward the Isfjorden (see MODIS imagery on <http://rapidfire.sci.gsfc.nasa.gov> at 18 May 2004 03:35 UTC and pictures at subsequent times covering Svalbard). Generally, events like this are more common in autumn, when most of Svalbard's valleys are free of snow. However, the dry and sunny conditions during the preceding weeks in April and May 2004 melted/evaporated the snow layer in the Adventdalen. Essentially, this particular flight track on 18 May 2004 was chosen to record the dispersion of the dust plume from its source region inside the valley to the mouth of the Isfjorden, see Fig. 3.

Figures 4 and 5 depict profiles of the averaged and high-pass filtered backscatter

Aerosol distribution around Svalbard

A. Dörnbrack et al.

Title Page

Abstract

Introduction

Conclusions

References

Tables

Figures

◀

▶

◀

▶

Back

Close

Full Screen / Esc

Printer-friendly Version

Interactive Discussion



ratio $R_{532\text{ nm}}$ and volume depolarization $\delta_{532\text{ nm}}$ taken at 17 selected segments along the flight track on 18 May 2004, for details see Table 1. We start our discussion with the profiles along the east-west section through the Advensdalen, shown in Fig. 4.

The profiles measured in the eastern part of the valley (Fig. 4a,b) show two distinct characteristics. The easternmost profile (number 17, black line) shows $R_{532\text{ nm}} > 100$ near the surface and an exponential decrease towards the ambient value of $R_{532\text{ nm}} \approx 1.4$ above 400 m over ground. This is the only profile containing data from a flight segment where the topographic height increased by about 250 m from near zero at the valley floor to its eastern part. Therefore, measurements at different heights above sea level (ASL) were averaged resulting in the rather thick aerosol layer, as shown in Fig. 4a. The volume depolarization of this particular profile is rather small with maximum values of $\delta_{532\text{ nm}}^{\text{MAX}} \approx 0.05$ (Fig. 4b). Both other profiles from the eastern part (number 15 and 16) exhibited elevated maxima of the backscatter ratio at around 500 m ASL whereby maximum backscatter ratios $R_{532\text{ nm}}^{\text{MAX}}$ decreased from 15 to about 5 along the mean flow direction toward west.

Inside the Adventdalen the vertical distribution of aerosol particles exhibited a different characteristics (Fig. 4c, d): large vertical $R_{532\text{ nm}}$ -gradients with $R_{532\text{ nm}} > 5$ near the surface and values close to 1.4 at the top of the aerosol layer point to a ground source. The volume depolarization of the respective profiles (numbers 10–14): $\delta_{532\text{ nm}}$ was always larger than 0.1 inside the aerosol layer and attained $\delta_{532\text{ nm}}^{\text{MAX}} \approx 0.3$ near the surface (Fig. 4d). Thus, the backscattering aerosol particles were aspherical and consisted most likely of mineral dust mobilized at the ground of the Adventdalen.

The aerosol layer thickened in flow direction along the valley towards the mouth of the Adventdalen, c.f. the sequence of $R_{532\text{ nm}}$ -profiles No 14–10 (from red to yellow in Fig. 4c). Simultaneously, the vertical $R_{532\text{ nm}}$ -gradient inside the aerosol layer became smaller. Eventually, over the open water of the Isfjorden, a well-mixed $R_{532\text{ nm}}$ -profile was established with values between 2 and 3 extending up to about 800 m altitude (the green profile No. 8 in Fig. 4c). The shape transition in the $R_{532\text{ nm}}$ and $\delta_{532\text{ nm}}$ -profiles from the source region inside the valley toward the Isfjorden indicates that the depolar-

Aerosol distribution around Svalbard

A. Dörnbrack et al.

Title Page

Abstract

Introduction

Conclusions

References

Tables

Figures

◀

▶

◀

▶

Back

Close

Full Screen / Esc

Printer-friendly Version

Interactive Discussion



ising dust particles were mixed upward.

Inside the Isfjorden, the $R_{532\text{ nm}}$ and $\delta_{532\text{ nm}}$ profiles No. 5–8, with exception of profile No. 9, which will be discussed later, still show the characteristics of a well-mixed aerosol layer (Fig. 5a, b). However, the height of this layer declined significantly downstream toward the mouth of the Isfjorden. Additionally, the gradually decreasing $R_{532\text{ nm}}$ -values indicate that the dust plume was diluted and dispersed along its way. As the values of $\delta_{532\text{ nm}}$ were greater than 0.1 inside the aerosol layer, we hypothesize that the observed aerosol particles predominantly consisted of the mineral dust mobilized and emitted in the Adventdalen.

However, the exceptionally large $R_{532\text{ nm}}$ -values at the location of profile No. 9 might tell a different story. This particular profile resulted from six overflights in a region which was impacted by the outflow of the Adventdalen, the strong flow past the mountain ridge north of it, and the glacier winds blowing over the Isfjorden further north of the mountains. Thus, both the $R_{532\text{ nm}}$ and the $\delta_{532\text{ nm}}$ -profiles might combine various aerosol sources and they are not representative for the dust plume exclusively originating from the Adventdalen.

The open sea profiles along the northwest-southeast oriented flight segments allow an estimate of the meridional gradients of the aerosol distribution in the lee of Svalbard, and in particular downstream of the Isfjorden. Figure 5c shows four profiles whereby the southernmost profile No 4 exhibits the lowest values of $R_{532\text{ nm}} < 2$ inside the boundary layer. The gradual growth of aerosol backscatter ratio from $R_{532\text{ nm}} \approx 2 \dots 3$ (northernmost profile No. 1) to $R_{532\text{ nm}} \approx 4 \dots 5$ (profile No. 3) indicates that the highest aerosol concentration was located downstream of the axis of the Isfjorden (see Fig. 3). The gradual reduction and the more pronounced decay of $R_{532\text{ nm}}$ with altitude towards north points to dilution of the plume due to mixing and sedimentation of the aerosol particles.

However, the most prominent feature of the profile No. 3 is the elevated strongly backscattering and depolarising aerosol layer ($R_{532\text{ nm}}^{\text{MAX}} > 50$, $\delta_{532\text{ nm}}^{\text{MAX}} > 1$) at around 600 m altitude. Most probably, this layer was produced by drifting ice crystals mobilized by

Aerosol distribution around Svalbard

A. Dörnbrack et al.

Title Page

Abstract

Introduction

Conclusions

References

Tables

Figures

◀

▶

◀

▶

Back

Close

Full Screen / Esc

Printer-friendly Version

Interactive Discussion



**Aerosol distribution
around Svalbard**

A. Dörnbrack et al.

[Title Page](#)[Abstract](#)[Introduction](#)[Conclusions](#)[References](#)[Tables](#)[Figures](#)[◀](#)[▶](#)[◀](#)[▶](#)[Back](#)[Close](#)[Full Screen / Esc](#)[Printer-friendly Version](#)[Interactive Discussion](#)

the strong easterly winds at the top of the coastal mountains. It is interesting to note that the southernmost profile No. 4 also exhibits a $R_{532\text{nm}}$ -maximum at about 750 m altitude. If one assumes that these drifting particles were emitted from the peaks of the mountains upstream (about 1200 m high and in a distance of 200 km), a mean airspeed of 10 m s^{-1} results in a rather realistic estimate of the thermal velocity of about -3 cm s^{-1} .

2.3 Lidar observations of 19 and 21 May 2004

One of the scientific goals of the two flights on 19 and 21 May 2004 was to map the meridional aerosol distribution in the lee of Svalbard under similar meteorological conditions as during the first flight by extending the observations toward north. Especially, we were interested in the fate of the dust plume. Furthermore, we expected a variation in the aerosol distribution from the calm wake region north of the Isfjord towards the predicted low-level jet at the northern tip of Svalbard (see Fig. 1b, c).

Figure 6 shows the time series of the backscatter ratio $R_{532\text{nm}}$ profiles along those legs which are marked in red in Fig. 1b and c, respectively. In each case, the starting point of the plotted flight segments was located in the warm wake region. In addition to $R_{532\text{nm}}$, two selected values of the range-corrected signal strength S (for the definition of the symbols, see Appendix A) were superimposed to mark the presence of strongly backscattering particles, i.e. of clouds in and above the marine boundary layer.

On 19 May 2004, the tropospheric aerosol concentration was generally low with $R_{532\text{nm}}^{\text{MAX}} \approx 1.4$ at altitudes greater 1000 m. The origin of the elevated area with the high backscatter ratio of $R_{532\text{nm}} \approx 5.5$ at 10:50 UTC cannot be resolved: Visual observations from the aircraft as well as satellite imagery as shown in Fig. 2 suggest the absence of visible clouds. However, the large volume depolarisation indicates that the cloud consisted most probably of ice particles.

Generally, the aerosol backscatter increased to values of $R_{532\text{nm}} \approx 3$ towards the sea surface. Backscatter ratio profiles with small vertical $R_{532\text{nm}}$ -gradients and surface

values of $R_{532\text{nm}}^{\text{MAX}}=2.6$ were mainly measured in the wake region west of Prins Karls Foreland between 10:30–11:00 UTC. Increased surface values $R_{532\text{nm}}\approx 4.0$ were observed in two distinct areas: in the vicinity of the northernmost way point at 10:15 UTC and near the mouth of the Isfjorden at around 11:15 UTC.

Both the triangular shape of the aerosol distribution and of the clouds (enhanced S -values) in the altitude-time cross-section constitute the prominent mesoscale feature of this flight segment. The obvious symmetry in the profiles results from the turning point of the aircraft at the apex of the triangle. These measurements reveal that the boundary layer height is increasing northward towards the ice edge. As the superimposed isentropes (black contour lines in Fig. 6) of the synoptic-scale meteorological analyses³ interpolated on the flight track reproduce the slope of the cloud layer remarkably well, it appears as possible to explain the unexpected boundary layer height growth.

On 19 May 2004 only one overflight across the tip jet was performed (see Fig. 1b). The success of the flight strategy encouraged us to perform another flight with two consecutive overflights of the coastal jet on 21 May 2004 (see Fig. 1c). The results depicted in Fig. 6b reveal the same mesoscale pattern of the aerosol distribution as found on 19 May 2004. However, as the wind speed was weaker on 21 May 2004 (Fig. 1c), the cloud top height was by about 200 m lower along the first passage of the low-level jet. Another reason for the lower boundary layer height is the enhanced thermal stratification (denser Θ -isolines) which suppressed the vertical aerosol transport. Besides the lower wind speeds on 21 May 2004, the low-level jet was also much more bended compared to the conditions on 19 May 2004 (see Fig. 1b and c). Therefore, the variation of the slope and the height of the mesoscale triangular patterns in downstream direction is hard to interpret. Furthermore, the northernmost way point of the second intersection of the low-level jet was further south. Thus, only the difference between the flights on 19 and 21 May 2004 gives evidence that the height of the aerosol layer is directly related to the surface wind speed.

³We use operational $T_{L511/L60}$ ECMWF analyses interpolated on a regular 0.5×0.5 latitude-longitude grid.

Aerosol distribution around Svalbard

A. Dörnbrack et al.

Title Page

Abstract

Introduction

Conclusions

References

Tables

Figures

◀

▶

◀

▶

Back

Close

Full Screen / Esc

Printer-friendly Version

Interactive Discussion



**Aerosol distribution
around Svalbard**

A. Dörnbrack et al.

[Title Page](#)[Abstract](#)[Introduction](#)[Conclusions](#)[References](#)[Tables](#)[Figures](#)[◀](#)[▶](#)[◀](#)[▶](#)[Back](#)[Close](#)[Full Screen / Esc](#)[Printer-friendly Version](#)[Interactive Discussion](#)

The dependence of the height of the simulated clouds on the horizontal wind speed and the thermal stratification can be also seen in the ECMWF's cloud liquid and cloud ice water content as shown in Fig. 7. Enhanced values of the simulated cloud condensate exist in those areas where the lidar measurements detected clouds at the top of the marine boundary layer or at higher levels on 21 May 2004: The high backscatter ratio above 1500 m between the triangularly shaped tip jet passages is partly related to clouds associated with the approaching warm front (see Figs. 1c, 2b).

It is most likely that the backscattering particles near the sea surface consisted predominantly of sea salt aerosols (Lewis and Schwartz, 2004). This was confirmed by the low depolarisation of the lidar observation. Additionally, mineral dust constituted a further possible source of aerosols west of the Isfjorden, especially for the measurements on 19 May 2004 when the dust storm in the Adventdalen still persisted, however, to a lesser strength.

3 Mesoscale numerical simulations

The observations presented in the preceding section show characteristic mesoscale features. These features are most likely the result of the flow distortion around Svalbard. Furthermore, the backscatter observations indicate at least two different local sources of aerosol particles. In this section, we test the hypothesis that the observed aerosol distribution can be explained by the mobilization of mineral dust and sea salt aerosols. For this purpose, we perform mesoscale numerical simulations of the flow past Svalbard including the transport of aerosols. In addition to dust and sea salt, ice particles emitted from the mountain ranges are included in the numerical simulations as visual observations indicated a strong snow and ice drift during the observation period.

3.1 Setup

Our numerical experiments were performed with the non-hydrostatic, anelastic model EULAG. An up-to-date comprehensive description of the model and its capabilities can be found in Prusa et al. (2008), Smolarkiewicz and Prusa (2005), and Prusa and Smolarkiewicz (2003). In Appendix B, the governing equations are summarized and the numerical procedure to solve them is described briefly.

In addition to the governing equations for mass, momentum and potential temperature, conservation equations for three passive scalars C^α ($\alpha=1, 2, 3$) are solved. For our simulations of the mobilization and transport of aerosol particles from and around Svalbard, we assign $\alpha=1$ to the concentration of mineral dust, $\alpha=2$ to sea salt, and $\alpha=3$ to ice crystals. In analogy to the turbulent surface fluxes of momentum and heat, we prescribe the turbulent surface flux of the respective scalar species C^α into the domain according to:

$$q^\alpha = \rho_0 u_* c_*^\alpha, \quad \alpha = 1, 2, 3 \quad (1)$$

where ρ_0 is density at the surface, $u_* = \kappa v_T / \log(z_{lm}/z_0)$ is the friction velocity with $\kappa=0.41$ as the von Karman constant, v_T is the magnitude of the tangential velocity at the lowest model level z_{lm} and z_0 is the roughness length. The quantity c_*^α denotes the effective amount of aerosols C^α mobilized at the model surface. In analogy to Ničković and Dobričić (1996) we prescribe c_*^α as follows:

$$c_*^\alpha = \begin{cases} 0 & \text{for } u_* < u_\tau^\alpha \\ C_{MAX}^\alpha \min \left[1, \left(\frac{u_*}{u_c^\alpha} \right)^3 \right] & \text{for } u_* > u_\tau^\alpha \end{cases}, \quad \alpha = 1, 2, 3 \quad (2)$$

where $C_{MAX}^\alpha = \rho^\alpha / \rho_0$ denotes the capacity of the atmosphere to accept the emitted material with density ρ^α from the surface (or, alternatively: the concentration potentially available for mobilization). The velocity u_c^α comprises a threshold and u_τ^α is the velocity at which the mobilization is initiated.

Title Page

Abstract

Introduction

Conclusions

References

Tables

Figures

◀

▶

◀

▶

Back

Close

Full Screen / Esc

Printer-friendly Version

Interactive Discussion



Aerosol distribution around Svalbard

A. Dörnbrack et al.

Title Page

Abstract

Introduction

Conclusions

References

Tables

Figures

◀

▶

◀

▶

Back

Close

Full Screen / Esc

Printer-friendly Version

Interactive Discussion



As we do not intend to perform a detailed and quantitative microphysical modelling of the aerosol mobilization and dispersion, we prescribe the following values for all scalar species: $u_c^\alpha = 1.2 \text{ ms}^{-1}$, $u_\tau^\alpha = 0.5 \text{ ms}^{-1}$, and $\rho^\alpha = 3.2 \cdot 10^{-3} \text{ kg}$. However, we restrict the source regions of the three aerosol components in such a way, that sea salt is emitted everywhere over open water south-west of the ice edge and in some fjords (e.g. Isfjorden). Dust is exclusively emitted from the Adventdalen, and ice particles are mobilized only over land at altitudes greater than 800 m.

3.2 Ambient states, initialisation, and boundary conditions

The governing equations are solved in a quadratic domain 718 km×718 km wide and 5 km high. We use 360×360×51 grid cells, i.e. $\Delta x = \Delta y = 2 \text{ km}$ and $\Delta z = 100 \text{ m}$. A realistic topographic model of Svalbard's islands is placed in the centre of the domain (see Fig. 9).

The environmental states for potential temperature $\theta_e = \theta_e(\mathbf{x}_c)$, and for the velocity components $\mathbf{v}_e = [u_e(\mathbf{x}_c), v_e(\mathbf{x}_c), 0]$ are obtained from upstream values of the ECMWF operational analyses at 30° E and 79° N valid on 19 May 2004 at 12:00 UTC, see the grey lines in Fig. 8. The respective background values for the scalars are set to zero. The initial conditions for the velocity components are \mathbf{v}_e and $\theta' = 0$. At the lower surface we specify a Neumann boundary conditions for momentum by assuming that the tangential stress is equal to a specified drag force τ_i :

$$\tau_i = \rho C_D |v_T| v_i, \quad i = 1, 2 \quad (3)$$

where v_i are the contravariant velocity components in the x - and y -directions, respectively and $C_D = 0.001$ is magnitude of the aerodynamical drag coefficient over flat surfaces and $C_D = 0.01$ over the rough mountains of Svalbard. Sensitivity experiments have been performed to test the influence of thermal convection on the aerosol distribution by prescribing a sensible surface heat flux of 20 and 40 W m^{-2} over the open water.

3.3 Numerical results

The simulated flow structure is illustrated by means of the horizontal distributions of potential temperature Θ and horizontal wind speed V_H at 800 m and 500 m altitude, respectively, see Fig. 9. After 18 h of simulation time, the descending flow in the wake region generates a positive temperature anomaly. Especially, the downstream development of the Θ -anomaly is in qualitative agreement with the satellite observations as shown in Fig. 2. A better quantitative comparison would require numerical simulations with realistic initial and evolving boundary conditions which is not the aim of our approach. In the numerical simulation with surface heat flux, the warm wake region is wider and extends further downstream. A characteristic feature of the simulated flow field are the numerous low-level jets streaming out of the individual fjords on Svalbard's west coast.

The associated aerosol distribution after 18 h simulation time is depicted at 300 m and 1200 m altitude in Fig. 10. There are three characteristic features: The dust, which was only emitted in the Adventdalen, propagates long distances downstream through the Isfjorden towards the Arctic Ocean. The dust plume broadens markedly towards north and retains a sharp gradient at its southern flank. Secondly, sea salt is emitted everywhere over open water if the friction velocity exceeds the threshold value of 0.5 ms^{-1} . Except in the calm wake region north of the Isfjorden, all other areas are filled with sea salt aerosols. At 300 m altitude, the strongest meridional gradients are simulated at the northern tip of Svalbard and at the exits of the fjords. A third characteristic feature is the dominance of ice crystals in the wake region. As ice crystals were only emitted at locations higher than 800 m, the presence of the tallest mountains of Svalbard just upstream is the most probable reason for the concentration maximum in the wake. Secondly, the induced vertical velocities associated with the flow past Svalbard lead to an efficient vertical mixing of the simulated particle concentration. Therefore, ice particles and to a lesser extent also dust is present at 1200 m altitude. In effect, only a tenth of the dust concentration can be found at 1200 m altitude whereas the ice

Aerosol distribution around Svalbard

A. Dörnbrack et al.

Title Page

Abstract

Introduction

Conclusions

References

Tables

Figures

◀

▶

◀

▶

Back

Close

Full Screen / Esc

Printer-friendly Version

Interactive Discussion



concentration is just a factor 3 smaller compared to the concentration at 300 m altitude. Based on our numerical simulations, only small amounts of sea salt can only be transported upward to 1200 m altitude by convective motions triggered by the positive sensible heat flux (see Fig. 10).

5 Figure 11 illustrates the vertical aerosol concentrations by means of two meridional cross sections located about 40 and 100 km downstream of Svalbard (see the respective baselines in Fig. 10). There are three regions of interest: Downstream of the Isfjorden (at $y \approx 350$ km in Fig. 11), high concentrations of all species are simulated in the marine boundary layer. In contrast, only ice crystals dominate the simulated aerosol
10 distribution in the wake region (between $y \approx 400$ and 500 km). Finally, the numerical simulations reveal an increase of sea salt aerosol concentration in the boundary layer further north at $y > 500$ km.

Large vertical Θ -gradients at the top of the boundary layer are also reflected in the aerosol plume downstream of the Isfjorden where the concentrations decrease
15 markedly with altitude. The simulated top height of the aerosol layer between 800 m and 1000 m is similar to the observed one. Obviously, the top and the shape of the aerosol plume is influenced by the presence of the warmer sea water: the top height increases by about 300 m in the simulation with surface sensible heat flux. Due to the predominantly vertical motions of the convective cells the aerosol plume is not as much
20 tilted northwards. Horizontally, sharp meridional gradients exist towards south whereas the northern flank of the aerosol plume shows a more gradual decrease.

The difference between the numerical simulations with and without sensible surface heat flux is most obvious in the isentropic surfaces in the wake region. In the simulation without surface heating the isentropes bend down due to the adiabatic descent
25 of the air passing over the mountains upstream. With surface heating, even with such small values of 20 and 40 W/m², a well-mixed boundary layer develops in the numerical simulations which counteracts the adiabatic descent. Although the surface heating influences the shape of the distribution of ice crystals in the wake region it does not influence the magnitude and gross vertical distribution. The absence of sea salt aerosols

Aerosol distribution around Svalbard

A. Dörnbrack et al.

[Title Page](#)[Abstract](#)[Introduction](#)[Conclusions](#)[References](#)[Tables](#)[Figures](#)[◀](#)[▶](#)[◀](#)[▶](#)[Back](#)[Close](#)[Full Screen / Esc](#)[Printer-friendly Version](#)[Interactive Discussion](#)

in the wake region is probably caused by the slow horizontal wind speeds which inhibit the mobilization of sea salt.

There is also an immense influence of the surface heating on the simulated sea salt aerosol distribution in the vicinity of the northern tip of Svalbard: no surface heating leads to slanted contour lines of the sea salt concentration and the shape resembles the observed triangular backscatter patterns from the lidar measurements (see Fig. 6). On the other hand, the surface heat flux triggers the vertical mixing more effectively and leads to an aerosol distribution typical for a convective mixing layer in regions of low V_H . Thus, we conclude that the observed triangular distribution is predominantly caused by the vertical motions associated with the high shear along the coastal jet.

Finally, vertical profiles at four selected locations represent the downstream evolution of Θ , V_H , and aerosol concentrations C_α along the Isfjorden for the two sets of simulations (Fig. 12). Starting with the easternmost profiles located at the elevated floor inside the Adventdalen (dash-dotted lines in Fig. 12), we see that the large wind speed mobilizes the dust in the valley. The strong shear $\partial V_H / \partial z$ leads to an effective vertical turbulent mixing of the dust concentration. Indeed, visual observations during the dust storm in Longyearbyen at 18 May 2004 evidenced that the sand and coal particles from the dry river bed along the valley were rapidly mixed up by the strong gusty winds.

At the next location – situated in the Isfjorden between the exits of the Adventdalen and the northwards located Sassendalen – (dashed lines in Fig. 12) we see the combining effects of the two airstreams: dust from the Adventdalen retains its maximum concentration between 500 and 1000 m altitude whereas the flow from the Sassendalen carries dust free air which lowers the aerosol concentration at lower levels. Additionally, sea salt aerosol particles are mobilized over the open water. The comparison of the total aerosol concentration at this location with the vertical profile No. 9 in Fig. 5a reveals an astonishing qualitative similarity.

Aerosol distribution around Svalbard

A. Dörnbrack et al.

Title Page

Abstract

Introduction

Conclusions

References

Tables

Figures

◀

▶

◀

▶

Back

Close

Full Screen / Esc

Printer-friendly Version

Interactive Discussion



4 Discussion and conclusions

During ASTAR 2004, a quasi-stationary weather situation caused strong easterly winds past Svalbard for a period of about four days. According to Skeie and Grønås (2000), easterly winds are dominating during the winter months rather than spring. This exceptional situation mid of May 2004 caused nearly cloud-free conditions in the lee of Svalbard's mountains. Airborne remote-sensing observations above and around the islands were performed to record the aerosol distribution emerging from the impact of the intense easterly winds. To our knowledge, these are the first lidar observations documenting the aerosol distribution in the lee of Svalbard under such a weather situation.

The series of lidar observations facilitated a study of the mobilization and the subsequent transport of the different aerosol particles along particular valleys and on the leeward side of the islands. For the first time, mesoscale aerosol features associated with the stable flow over Svalbard could be visualized in the lidar data. Most of the published aerosol lidar observations are performed by ground-based stations under calm high-pressure and clear-sky conditions. Therefore, our airborne remote-sensing observations add new insights about the spatial aerosol distribution in the Svalbard area.

Advantageously, the low background concentration of anthropogenic aerosols during this particular period enabled the identification of the sources of the backscattering particles by a combination of remote-sensing observations and mesoscale numerical modelling: Most of the observed backscattering particles were produced by local sources and consisted either of mineral dust, sea salt, or ice crystals. Exceptionally for the time of the year, mineral dust and soot particles were mobilized from the surface of the almost snow-free Adventsdalen on 18 and 19 May 2004. Visual observations as well as satellite imagery document this unique event impressively. Our airborne lidar observations show the upward transport of aerosol particles and the evolution of a well-mixed aerosol layer along its way toward the open sea (Fig. 4c). The high backscatter values and the volume depolarisation greater 10% in this layer confirm that most of the

Aerosol distribution around Svalbard

A. Dörnbrack et al.

Title Page

Abstract

Introduction

Conclusions

References

Tables

Figures

◀

▶

◀

▶

Back

Close

Full Screen / Esc

Printer-friendly Version

Interactive Discussion



backscattering particles consisted of mineral dust. Furthermore, the numerical simulations represent the evolution of the mixed layer in the Adventsdalen qualitatively.

Over the open water of the Isfjorden, the further fate of the dust plume was characterized by dilution. Due to sedimentation the height of the aerosol plume decreased along its downstream evolution. This behavior is also reflected in the numerical simulations. Additionally, the backscatter and the depolarisation measurements as well as the numerical simulations indicate that the observed plume over the Isfjorden contained sea salt and ice particles.

Whereas the airborne observations over the Isfjorden on 18 May 2004 reveal a mix of different backscattering aerosol particles, the conditions during the both flights on 19 and 21 May 2004 in the lee and north of Svalbard identify sea salt as the dominant backscattering aerosol inside the marine boundary layer. The numerical simulations reveal that the height of the sea spray contamination depends on the surface wind speed and the characteristic triangular shape was generated due to the combined action of descending air in the lee of the mountains and the ascent in the low-level jet. There, the vertical shear of the horizontal wind speed created streamwise vortices that lead to an unusual growth of the boundary layer height towards the ice edge.

Generally, our airborne lidar observations and the numerical simulations indicate that a significant source of aerosols in the Svalbard area is sea salt which is ejected by different physical processes into the marine boundary layer (see Hara et al., 2003). It is beyond the scope of the present paper to study the sea salt flux in detail as done by Clarke et al. (2006). Extensive remote-sensing and in-situ observations are necessary to undertake such an assessment. However, we point out that sea spray is a significant local source on Svalbard, especially, in years when the sea ice is shifted towards north and the coastal areas are free of ice. But not only the ejection from breaking water waves is a source of sea salt. Recent studies of Yang et al. (2008) have shown that snow lying in sea ice could be a potentially important source of sea salt as well.

It is not clear if local sources play a significant role in the overall aerosol characteristics in the Svalbard area. Certainly, events like the one presented in this paper do

Aerosol distribution around Svalbard

A. Dörnbrack et al.

[Title Page](#)[Abstract](#)[Introduction](#)[Conclusions](#)[References](#)[Tables](#)[Figures](#)[◀](#)[▶](#)[◀](#)[▶](#)[Back](#)[Close](#)[Full Screen / Esc](#)[Printer-friendly Version](#)[Interactive Discussion](#)

not occur frequently. However, if the meteorological situations are enforcing a strong flow past Svalbard, the aerosol distributions above and around the islands are strongly dependent on the local factors as topography, heat content of the water and the upstream wind direction. Climate models often use averaged profiles from stations in the vicinity of orography. How these profiles are to account for topographic effects under certain meteorological conditions remains an open issue. For this reason, it would be worthwhile to have simultaneous quantitative in-situ observations of the aerosol properties in addition to the lidar profile in order to simulate the aerosol evolution with more advanced micro-physical models.

Appendix A

AMALi

The nadir-aiming eye-safe Airborne Mobile Aerosol Lidar (AMALi) utilized a Nd:Yag laser operating with 15 Hz repetition rate at a linearly polarised wavelength of 532 nm and with a pulse energy of 120 mJ. The large laser beam divergence of 2.6 mrad ensured the eye-safety beyond distances greater than 2.5 km off the system. The parabolic off-axis mirror with a field of view of 3.1 mrad was employed and provided a small range of geometrical compression of 245 m. The range of airborne measurements was limited to the maximum nominal operation height for the laser of 3 km altitude above sea level. This short vertical range assured sufficiently high signal-to-noise ratio (SNR) and allowed the photo-multipliers to operate in an analog mode.

Airborne lidar applications require short integration times in order to achieve sufficient horizontal resolution. During ASTAR 2004, an acceptable SNR was already achieved for an integration time of 1 s corresponding to a horizontal resolution between 46 m and 77 m depending on the aircraft ground speed between 166 kmh^{-1} (90 kt) and 278 kmh^{-1} (150 kt), respectively.

In this paper, we use the following two values to characterize the tropospheric aerosol

Aerosol distribution around Svalbard

A. Dörnbrack et al.

Title Page

Abstract

Introduction

Conclusions

References

Tables

Figures

◀

▶

◀

▶

Back

Close

Full Screen / Esc

Printer-friendly Version

Interactive Discussion



Aerosol distribution around Svalbard

A. Dörnbrack et al.

Title Page

Abstract

Introduction

Conclusions

References

Tables

Figures

◀

▶

◀

▶

Back

Close

Full Screen / Esc

Printer-friendly Version

Interactive Discussion



properties: the backscatter ratio $R_{532\text{ nm}} = \frac{\beta_{\text{part}} + \beta_{\text{mol}}}{\beta_{\text{mol}}}$, whereby β_{part} is the backscatter coefficient due to particles and β_{mol} the backscatter coefficient due to molecules. Secondly, the range-corrected signal strength $S(h) = P(h) \cdot h^2$, whereby $P(h)$ denotes the intensity of the measured current at the range h , is used to mark the boundaries of clouds. All the observed profiles were averaged over 15 s with range resolution of 7.5 m and horizontal resolution of 1 km for typical aircraft ground speed of 130 kt. The average length of a typical airborne profile varied between 2.5 and 2.7 km depending on flight altitude and taking into account the losses due to geometrical compression near the lidar.

The backscatter profiles were obtained by a combination of the Klett-Fernald evaluation scheme (Klett, 1981, 1985; Fernald, 1984) with the classic Newton-Raphson iterative method, and calibrated with a newly developed two-stream algorithm (Stachlewska et al., 2005, Ritter et al., 2006). A detailed description of the AMALi construction, design and evaluation schemes can be found in Stachlewska et al. (2004).

Appendix B

The numerical model EULAG

The governing equations are formulated for the Cartesian velocity components $\mathbf{v} = (u, v, w)$ as a function of curvilinear coordinates (x, y, z) which are related to the Cartesian coordinates (x_c, y_c, z_c) according to the transformation $[x, y, z] = [x_c, y_c, \eta(x_c, y_c, z_c)]$. Here,

$$\eta = H \frac{z_c - h}{H - h} \quad (\text{B1})$$

maps the domain above an undulated surface at height $h(x_c, y_c)$ and below a plane top surface at $z = H$ onto a rectangular transformed domain. The coordinate transform

enters the governing equations of motion through the metric coefficients

$$G^{ij} = \sum_{k=1}^m \frac{\partial x^i}{\partial x_c^k} \frac{\partial x^j}{\partial x_c^k}, \quad (\text{B2})$$

and the Jacobian of the transformation $G = (\det\{G^{ij}\})^{-1/2}$. The anelastic equations are written in the following form (cf. Smolarkiewicz and Margolin, 1997):

$$\frac{\partial \rho^* u_j}{\partial x_j} = 0, \quad (\text{B3})$$

$$\frac{du}{dt} = -\frac{\partial \pi}{\partial x} - G^{13} \frac{\partial \pi}{\partial z} + f v' - \mathcal{D}_1(e, \nabla \mathbf{v}) - \alpha_m u', \quad (\text{B4})$$

$$\frac{dv}{dt} = -\frac{\partial \pi}{\partial y} - G^{23} \frac{\partial \pi}{\partial z} - f u' - \mathcal{D}_2(e, \nabla \mathbf{v}) - \alpha_m v', \quad (\text{B5})$$

$$\frac{dw}{dt} = -\frac{1}{G} \frac{\partial \pi}{\partial z} + g \frac{\theta'}{\theta} - \mathcal{D}_3(e, \nabla \mathbf{v}) - \alpha_m w, \quad (\text{B6})$$

$$\frac{d\theta'}{dt} = -v_j^* \frac{\partial \theta_e}{\partial x_j} - \mathcal{D}_h(e, \nabla \theta) - \alpha_h \theta', \quad (\text{B7})$$

$$\frac{dC^\alpha}{dt} = -\mathcal{D}_c^\alpha(e, \nabla C^\alpha), \quad \alpha = 1, 2, 3, \quad (\text{B8})$$

$$\frac{de}{dt} = S(e), \quad (\text{B9})$$

where θ is the potential temperature, C^α denote the scalar species, ρ^* is the reference density $\bar{\rho}$ multiplied by the Jacobian of coordinate transformation, π is the pressure perturbation with respect to the undisturbed environmental profile normalized by $\bar{\rho}$, f is the Coriolis parameter, and g is the acceleration due to gravity. The total derivative is given by $d./dt = \partial./\partial t + \nabla \bullet (\rho^* .)$ with $\nabla := (\partial/\partial x, \partial/\partial y, \partial/\partial z)$. Primed variables denote the

Aerosol distribution around Svalbard

A. Dörnbrack et al.

Title Page

Abstract

Introduction

Conclusions

References

Tables

Figures

◀

▶

◀

▶

Back

Close

Full Screen / Esc

Printer-friendly Version

Interactive Discussion



deviations to an undisturbed environmental state θ_e , u_e , and v_e . The attenuation forcings with coefficients α_m and α_h appearing in the momentum and entropy equations simulate wave-absorbing devices in the vicinity of the open lateral boundaries of the numerical model.

5 The \mathcal{D} -terms appearing in the above equations symbolize viscous dissipation of momentum, diffusion of heat and species via the divergence of turbulent stresses and fluxes of heat and species, respectively.

$$\mathcal{D}_i = \frac{\partial \tau_{ij}}{\partial x_j}, \quad \tau_{ij} = 2\rho K_M \left(e_{ij} - \frac{1}{3} \delta^{ij} e_{kk} \right), \quad (\text{B10})$$

$$\mathcal{D}_h = \rho K_H \delta^{ij} \frac{\partial \theta}{\partial x_j} \quad (\text{B11})$$

$$10 \quad \mathcal{D}_c^\alpha = \rho K_H \delta^{ij} \frac{\partial C^\alpha}{\partial x_j} \quad (\text{B12})$$

where

$$e_{ij} = \frac{1}{2} \left(\frac{\partial u_i}{\partial x_j} + \frac{\partial u_j}{\partial x_i} \right) \quad (\text{B13})$$

is the rate-of-strain tensor. For a detailed description of the diffusive terms in time-dependent curvilinear coordinates, see Prusa and Smolarkiewicz (2003). The corresponding eddy coefficients K_M and K_H are proportional to the square root of the turbulent kinetic energy e . In the subgrid-scale (SGS) model all sources and sinks of e are combined in $\mathcal{S}(e)$; see Sorbjan 1996 and Margolin et al., 1999 for details of the SGS-model.

20 The governing equations are solved by means of finite-difference approximations using a second-order accurate nonoscillatory forward-in-time (NFT) approach (Smolarkiewicz and Margolin, 1997; Smolarkiewicz and Prusa, 2005). The prognostic equa-

**Aerosol distribution
around Svalbard**

A. Dörnbrack et al.

Title Page

Abstract

Introduction

Conclusions

References

Tables

Figures

◀

▶

◀

▶

Back

Close

Full Screen / Esc

Printer-friendly Version

Interactive Discussion



tions are written compactly in a conservation-law form

$$\frac{\partial \rho^* \Psi}{\partial t} + \nabla \cdot (\rho^* \mathbf{v} \Psi) = \rho^* R^\Psi, \quad (\text{B14})$$

where Ψ symbolizes the velocity components u , v , and w , the passive scalars C^α , the potential temperature θ or the turbulent kinetic energy e . On a discrete mesh, the NFT approximation of Eq. (B14) can be written as

$$\Psi_i^{n+1} = LE_i(\tilde{\Psi}) + 0.5\Delta t R_i^\Psi|^{n+1}, \quad (\text{B15})$$

where Ψ_i^{n+1} denotes the solution at the grid point (t^{n+1}, \mathbf{x}_i) , $\tilde{\Psi} := \Psi^n + 0.5\Delta t R^\Psi|^{n+1}$, and LE denotes the NFT transport operator. In the Eulerian scheme, used exclusively in this paper, LE integrates the homogeneous transport Eq. (B14) — viz., LE advects $\tilde{\Psi}$ using a fully second-order-accurate flux-form scheme MPDATA (for a review, see Smolarkiewicz and Margolin, 1998).

The SGS forcings included in R^Ψ are evaluated explicitly and to the first order. This is justified because the \mathcal{D} -terms enter the governing equations only as a consequence of a SGS turbulence model, i.e. already as a correction $\mathcal{O}(\Delta x)$. Technically, this eliminates the need for predicting SGS^{n+1} in $R^\Psi|^{n+1}$ on the rhs of Eq. (B15), as $SGS(\Psi^{n+1}) = SGS(\Psi^n) + \mathcal{O}(\Delta t)$. Technically, the definition of the auxiliary field $\tilde{\Psi}$ is expanded as $\tilde{\Psi} := \Psi^n + 0.5\Delta t (R_{inv}^\Psi|^{n+1} + 2R_{SGS}^\Psi|^{n+1})$. Here, the resolved inviscid forcings are accounted for in $R_{inv}^\Psi|^{n+1}$ in $R^\Psi|^{n+1}$ on the rhs of Eq. (B15); refer to Sects. 3.5.4 and 4.3 in Smolarkiewicz and Margolin (1998). The explicit first-order evaluation of the SGS forcings improves the efficacy of the numerical calculations.

In the implicit option of the model algorithm, $\Psi \equiv \theta'$ the entropy equation is solved simultaneously with the momentum equations – via formulating and solving an elaborate elliptic problem for pressure, cf. Smolarkiewicz et al. (2004) for discussion – whereupon the buoyancy term is integrated implicitly over $t \in [t^n, t^{n+1}]$ using the trapezoidal rule (see Dörnbrack et al., 2005).

Aerosol distribution around Svalbard

A. Dörnbrack et al.

Title Page

Abstract

Introduction

Conclusions

References

Tables

Figures

◀

▶

◀

▶

Back

Close

Full Screen / Esc

Printer-friendly Version

Interactive Discussion



References

- Clarke, A. D., Owens, S. R., and Zhou, J.: An ultra-fine sea-salt flux from breaking waves: Implications for cloud condensation nuclei in the remote marine atmosphere, *J. Geophys. Res.*, 111, D06202, doi:10.1029/2005JD006565, 2006.
- 5 Dörnbrack, A., Doyle, J. D., Lane, T. P., Sharman, R. D., and Smolarkiewicz, P. K.: On physical realizability and uncertainty of numerical solutions, *Atmos. Sci. Lett.*, 6, 118–122, 2005.
- Doyle, J. D. and Shapiro, M. A.: Flow response to large-scale topography: the Greenland tip jet, *Tellus*, 51A, 728–748, 1999.
- Engvall, A.-C., Krejci, R., Ström, J., Minikin, A., Treffeisen, R., Stohl, A., and Herber, A.: In-situ airborne observations of the microphysical properties of the Arctic tropospheric aerosol during late spring and summer, *Tellus B*, 60, 392–404, 2008.
- 10 Fernald, F. G.: Analysis of atmospheric lidar observations: some comments, *Appl. Opt.*, 23, 652–653, 1984.
- Garrett, T. J., Radke, L. F., and Hobbs, P. V.: Aerosol effects on cloud emissivity and surface longwave heating in the Arctic, *J. Atmos. Sci.*, 59, 769–778, 2002.
- 15 Hara, K., Yamagata, S., Yamanouchi, T., Sato, K., Herber, A., Iwasaka, Y., Nagatani, M., and Nakata, H.: Mixing states of individual aerosol particles in spring Arctic troposphere during ASTAR 2000 campaign, *J. Geophys. Res.*, 108(D7), 4209, doi:10.1029/2002JD002513, 2003.
- 20 Klett, J. D.: Stable analytical inversion solution for processing lidar returns, *Appl. Opt.*, 20, 211–220, 1981.
- Klett, J. D.: Lidar inversions with variable backscatter/extinction values, *Appl. Opt.*, 24, 211–220, 1985.
- Lewis, E. R. and Schwartz, S. E.: *Sea Salt Aerosol Production: Mechanisms, Methods, Measurements, and Models – A Critical Review*, American Geophysical Union, Washington, DC, *Geophys. Monogr.*, 152, 413 pp., 2004.
- 25 Lubin, D. and Vogelmann, A. M.: A climatologically significant aerosol longwave indirect effect in the Arctic, *Nature*, 439, 453–456, 2006.
- Margolin, L. G., Smolarkiewicz, P. K., and Sorbjan, Z.: Large-eddy simulations of convective boundary layers using nonoscillatory differencing, *Physica D.*, 133, 390–397, 1999.
- 30 Ničković, S. and Dobričić, S.: A model for long-range transport of desert dust, *Mon. Weather Rev.*, 124, 2537–2544, 1996.

Aerosol distribution around Svalbard

A. Dörnbrack et al.

Title Page

Abstract

Introduction

Conclusions

References

Tables

Figures

◀

▶

◀

▶

Back

Close

Full Screen / Esc

Printer-friendly Version

Interactive Discussion



**Aerosol distribution
around Svalbard**

A. Dörnbrack et al.

[Title Page](#)[Abstract](#)[Introduction](#)[Conclusions](#)[References](#)[Tables](#)[Figures](#)[◀](#)[▶](#)[◀](#)[▶](#)[Back](#)[Close](#)[Full Screen / Esc](#)[Printer-friendly Version](#)[Interactive Discussion](#)

- Orr, A., Hunt, J., Capon, R., Sommeria, J., Cresswell, D., and Owinoh, A.: Coriolis effects on wind jets and cloudiness along coasts, *Weather*, 60, 291–299, 2005.
- Pickart, R. S., Spall, M. A., Ribergaard, M. H., Moore, G. W. K., and Milliff, R. F.: Deep convection in the Irminger Sea forced by the Greenland tip jet, *Nature*, 424, 152–156, 2003.
- 5 Pierrehumbert, R. T.: Stratified ageostrophic flow over two-dimensional topography in an unbounded atmosphere, *J. Atmos. Sci.*, 42, 523–526, 1985.
- Prusa, J. M. and Smolarkiewicz, P. K.: An all-scale anelastic model for geophysical flows: dynamic grid deformation, *J. Comp. Phys.*, 190, 601–622, 2003.
- Prusa, J. M., Smolarkiewicz, P. K., and Wyszogradski, A. A: EULAG, a computational model for
10 multiscale flows, *Computer & Fluids*, 37, 1193–1207, 2008.
- Radke, L. F., Lyons, J. H., Hegg, D. A., Hobbs, P. V., and Bailey, I. H.: Airborne observations of arctic aerosols.1: Characteristics of Arctic haze, *Geophys. Res. Lett.*, 11, 393–396, 1984.
- Rinke, A., Dethloff, K., and Fortmann, M.: Regional climate effects of Arctic haze, *Geophys. Res. Lett.*, 31, L16202, doi:10.1029/2004GL020318r, 2004.
- 15 Ritter C., Notholt, J., Fischer, J., and Rathke, C.: Direct thermal radiative forcing of tropospheric aerosol in the Arctic measured by ground based infrared spectrometry, *Geophys. Res. Lett.*, 32, L23816, doi:10.1029/2005GL024331, 2005.
- Ritter, C., Stachlewska, I. S., and Neuber, R.: Application of the two-stream evaluation for a case study of Arctic Haze over Spitsbergen, in *Proceedings of 23rd International Laser Radar Conference (ILRC 2006 in Nara, Japan)*, edited by: Nagasawa, C. and Sugimoto, N., 20 1, 507–510, ISBN 4-9902916-0-3, 2006.
- Sandvik, A. D. and Furevik, B. R.: Case study of a coastal jet at Spitsbergen – Comparison of SAR- and model-estimated wind, *Mon. Weather Rev.*, 130, 1040–1051, 2002.
- Schär, C.: Mesoscale mountains and the large-scale atmospheric dynamics: A review, in: *Meteorology at the Millenium*, Academic Press, 29–42, 2002.
- 25 Schnell, R. C.: Arctic haze and the ARCTIC GAS AND AEROSOL SAMPLING PROGRAM (AGASP), *Geophys. Res. Lett.*, 11, 361–364, 1984.
- Schnell, R. C., Barry, R. G., Miles, M. W., Andreas, E. L., Radke, L. F., Brockm, C. A., McCormick, M. P., and Moore, J. L.: Lidar detection of leads in Arctic sea ice, *Nature*, 359, 530–532, 1989.
- 30 Schwartz, S. E. and Andreae, M. O.: Uncertainty in climate change caused by aerosols, *Science*, 272, 1121–1122, 1996.
- Skeie, P. and Grønås, S.: Strongly stratified easterly flows across Spitsbergen, *Tellus*, 52A,

473–486, 2000.

Smolarkiewicz, P. K. and Margolin, L. G.: On forward-in-time differencing for fluids: An Eulerian/semi-Lagrangian nonhydrostatic model for stratified flows, *Atmos. Ocean Special*, 35, 127–152, 1997.

5 Smolarkiewicz, P. K. and Margolin, L. G.: MPDATA: A finite-difference solver for geophysical flows, *J. Comput. Phys.*, 140, 459–480, 1998.

Smolarkiewicz, P. K., Temperton, C., Thomas, S. J., and Wyszogrodzki, A. A.: Spectral Preconditioners for nonhydrostatic atmospheric models: extreme applications, ECMWF Seminar Series on *Recent developments in numerical methods for atmospheric and ocean modelling*, 6–10 September 2004, Reading, UK (online: <http://www.ecmwf.int/publications/library>), 2004.

Smolarkiewicz, P. K. and Prusa, J. M.: Towards mesh adaptivity for geophysical turbulence: continuous mapping approach, *Int. J. Numer. Meth. Fluids*, 47, 789–801, 2005.

15 Sorbjan, Z.: Numerical study of penetrative and “solid lid” nonpenetrative convective boundary layers, *J. Atmos. Sci.*, 53, 101–112, 1996.

Stachlewska, I. S., Wehrle, G., Stein, B., and Neuber, R.: Airborne Mobile Aerosol Lidar for measurements of Arctic aerosols, *Reviewed Papers 22nd ILRC, ESA, SP-561*, 1, 87–89, 2004.

20 Stachlewska, I. S., Ritter, C., and Neuber, R.: Application of the two-stream inversion algorithm for retrieval of extinction, backscatter and lidar ratio for clean and polluted Arctic air, in *Proceedings of SPIE*, Vol. 5584, 03/1–03/8, 2005.

Thomason, L. W., Herber, A. B., Yamanouchi, T., and Sato, K.: Arctic study on tropospheric aerosol and radiation: comparison of tropospheric aerosol extinction profiles measured by airborne photometer and SAGE II, *Geophys. Res. Lett.*, 30, L1328, doi:10.1029/2002GL016453, 2003.

25 Treffeisen, R., Herber, A., Ström, J., Shiobara, M., Yamanouchi, T., Yamagata, S., Holmen, K., Kriews, M., and Schrems, O.: Interpretation of Arctic aerosol properties using cluster analysis applied to observations in the Svalbard area, *Tellus*, 56B, 457–476, 2004.

30 Yamanouchi, T., Treffeisen, R., Herber, A., Shiobara, M., Yamagata, S., Hara, K., Sato, K., Yabuki, M., Tomikawa, Y., Rinke, A., Neuber, R., Schumacher, R., Kriews, M., Ström, J., Schrems, O., and Gernhardt, H.: Arctic study of tropospheric aerosol and radiation (ASTAR) 2000: Arctic haze case study, *Tellus*, 57B, 141–152, 2005.

ACPD

9, 16441–16481, 2009

Aerosol distribution around Svalbard

A. Dörnbrack et al.

Title Page

Abstract

Introduction

Conclusions

References

Tables

Figures

◀

▶

◀

▶

Back

Close

Full Screen / Esc

Printer-friendly Version

Interactive Discussion



Yang, X., Pyle, J. A., and Cox, R. A.: Sea salt aerosol production and bromine release: Role of snow on ice, *Geophys. Res. Lett.*, 35, L16815, doi:10.1029/2008GL034536, 2008.

ACPD

9, 16441–16481, 2009

Aerosol distribution around Svalbard

A. Dörnbrack et al.

Title Page

Abstract

Introduction

Conclusions

References

Tables

Figures

◀

▶

◀

▶

Back

Close

Full Screen / Esc

Printer-friendly Version

Interactive Discussion



Aerosol distribution around Svalbard

A. Dörnbrack et al.

Table 1. Locations of the 17 areas where the vertical aerosol backscatter and depolarization profiles were calculated. The area number refers to the colored boxes in Fig. 3. This table lists the coordinates of the respective areas and the observation times of the AMALi observations that were used to average the vertical backscatter and depolarization profiles as shown in Figs. 4 and 5.

| Area No | $\lambda_{\text{MIN}}/\lambda_{\text{MAX}}$ | $\phi_{\text{MIN}}/\phi_{\text{MAX}}$ | Times/UTC |
|---------|---|---------------------------------------|---|
| 1 | 11.58° E/11.65° E | 77.93° N/77.97° N | 11:01:19–11:02:09, 11:33:24–11:33:47 |
| 2 | 11.79° E/11.86° E | 77.87° N/77.91° N | 10:59:39–11:00:09, 11:35:13–11:35:46 |
| 3 | 11.93° E/12.00° E | 77.84° N/77.88° N | 10:58:23–10:59:02, 11:36:24–11:36:57 |
| 4 | 12.29° E/12.36° E | 77.76° N/77.78° N | 11:39:29–11:40:04, 11:51:56–11:52:29 |
| 5 | 13.30° E/13.70° E | 78.00° N/78.17° N | 10:44:01–10:47:10, 12:02:23–12:05:10 |
| 6 | 14.10° E/14.50° E | 78.15° N/78.25° N | 10:38:12–10:40:49, 12:07:44–12:10:17 |
| 7 | 14.95° E/15.11° E | 78.27° N/78.29° N | 10:34:32–10:35:27, 12:13:09–12:14:06 |
| 8 | 15.11° E/15.24° E | 78.28° N/78.30° N | 10:33:51–10:34:30, 12:14:08–12:14:20 12:32:35–12:32:42 |
| 9 | 15.20° E/15.38° E | 78.31° N/78.34° N | 09:14:35–09:15:31, 09:20:08–09:21:04 10:00:39–10:01:37, 10:07:36–10:08:09 10:25:20–10:26:12, 10:32:19–10:33:09 |
| 10 | 15.39° E/15.42° E | 78.28° N/78.31° N | 09:21:48–09:22:00, 09:43:12–09:43:30 09:43:42–09:43:51, 10:00:09–10:00:27 10:08:24–10:08:29, 10:24:28–10:24:28 |
| 11 | 15.52° E/15.62° E | 78.22° N/78.28° N | 09:22:49–09:23:35, 09:44:54–09:45:36 09:58:07–09:59:03, 10:09:53–10:10:49 10:22:28–10:23:07, 12:16:48–12:17:33 12:29:40–12:30:17 |

[Title Page](#)
[Abstract](#)
[Introduction](#)
[Conclusions](#)
[References](#)
[Tables](#)
[Figures](#)
[Back](#)
[Close](#)
[Full Screen / Esc](#)
[Printer-friendly Version](#)
[Interactive Discussion](#)


Aerosol distribution around Svalbard

A. Dörnbrack et al.

Table 1. Continued.

| Area No | $\lambda_{\text{MIN}}/\lambda_{\text{MAX}}$ | $\phi_{\text{MIN}}/\phi_{\text{MAX}}$ | Times/UTC |
|---------|---|---------------------------------------|---|
| 12 | 15.62° E/15.72° E | 78.21° N/78.25° N | 09:23:36–09:24:16, 09:45:37–09:46:20 09:57:22–09:58:05, 10:10:51–10:11:44 10:21:55–10:22:27, 12:17:35–12:18:14 12:29:03–12:29:39 |
| 13 | 15.72° E/15.82° E | 78.19° N/78.22° N | 09:24:54–09:24:55, 09:46:21–09:47:02 09:56:43–09:57:21, 10:11:45–10:12:27 10:21:20–10:21:53, 10:18:15–10:18:55 12:28:24–12:29:02 |
| 14 | 15.82° E/15.88° E | 78.19° N/78.20° N | 09:27:04–09:27:26, 09:56:23–09:56:42 10:12:28–10:12:48, 10:20:57–10:21:19 12:18:56–12:19:20, 12:28:00–12:28:23 |
| 15 | 15.94° E/16.08° E | 78.17° N/78.22° N | 09:25:43–09:26:35, 09:47:50–09:48:43 09:55:07–09:55:58, 10:13:10–10:14:00 10:19:30–10:20:25, 12:19:45–12:20:34 12:26:45–12:27:33 |
| 16 | 16.08° E/16.18° E | 78.17° N/78.18° N | 09:54:50–09:55:05, 10:14:12–10:14:31 12:20:35–12:20:55 |
| 17 | 16:30° E/16:45° E | 78.19° N/78.20° N | 09:50:00–09:50:50, 09:52:59–09:53:48 10:15:24–10:16:15, 10:17:16–10:17:52 12:21:52–12:22:40, 12:24:43–12:25:28 |

Title Page

Abstract

Introduction

Conclusions

References

Tables

Figures

◀

▶

◀

▶

Back

Close

Full Screen / Esc

Printer-friendly Version

Interactive Discussion



Aerosol distribution
around Svalbard

A. Dörnbrack et al.

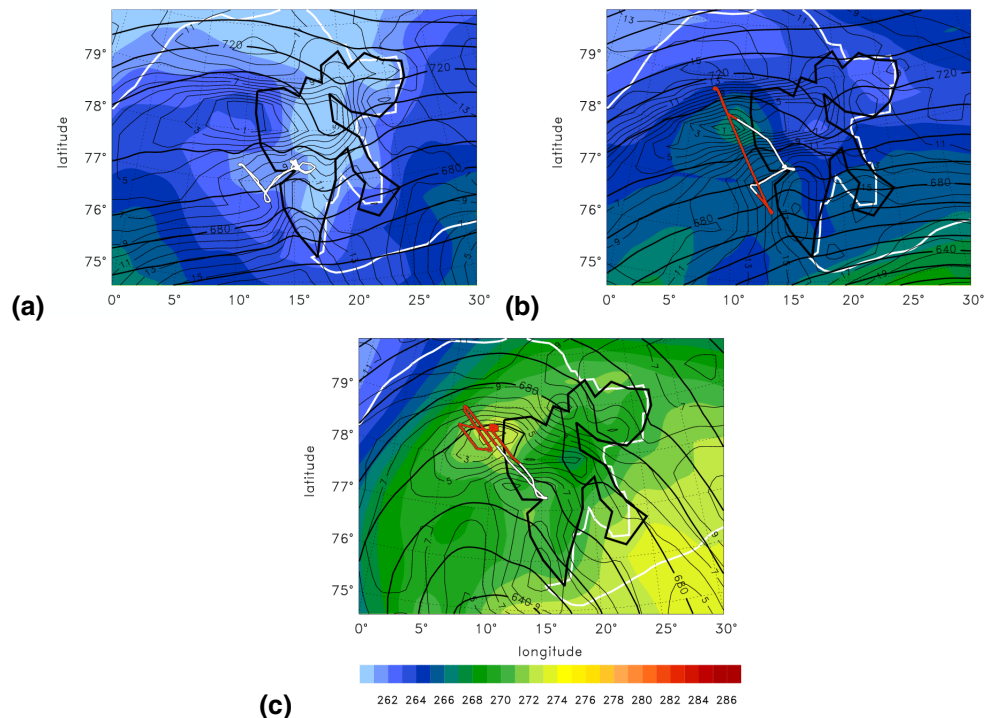


Fig. 1. Temperature (K, color shaded), geopotential height (m; thick solid lines), and horizontal wind speed (ms^{-1} , thin solid lines) on the 925 hPa pressure surface at 18 May 2004 12:00 UTC **(a)**, 19 May 2004 12:00 UTC **(b)**, and at 21 May 2004 18:00 UTC **(c)**. Data are operational T511/L60 ECMWF analyses interpolated on a regular 0.5×0.5 latitude-longitude grid. The thick white line marks the analysed ice edge. The flight paths of the Polar 2 research aircraft are marked by white/red lines.

Title Page

Abstract

Introduction

Conclusions

References

Tables

Figures

◀

▶

◀

▶

Back

Close

Full Screen / Esc

Printer-friendly Version

Interactive Discussion



**Aerosol distribution
around Svalbard**

A. Dörnbrack et al.

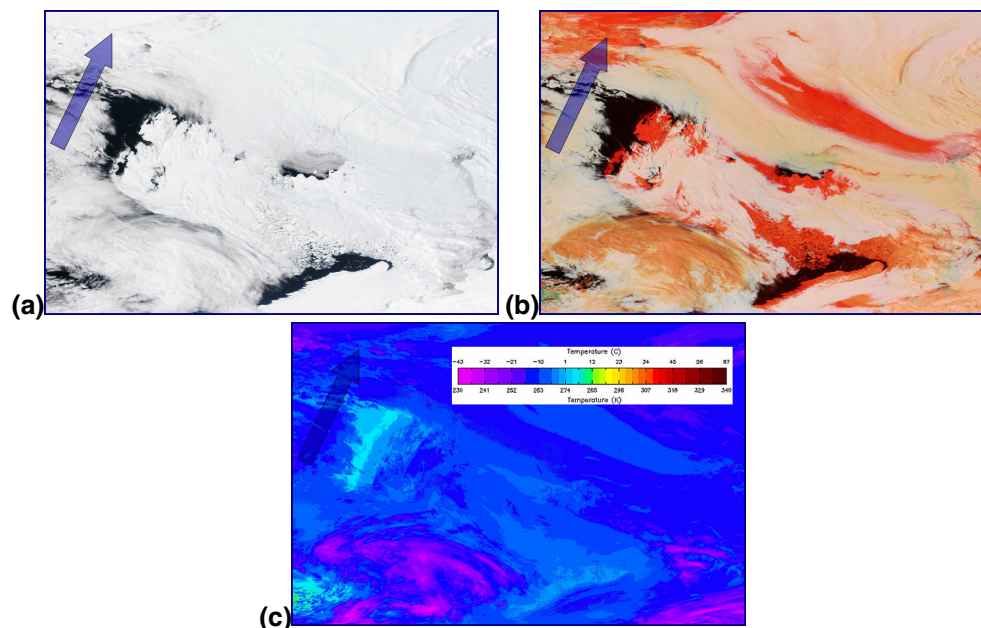


Fig. 2. MODIS satellite imagery of channels 1, 4, 3 (670 nm, 565 nm, and 479 nm) so-called true color **(a)**, of channels 3, 6, 7 (479 nm, 1.652 nm, and 2.155 nm) the red colors **(b)**, and the land surface temperature **(c)** valid on 19 May 2004 at 09:05 UTC. In the red channels ice and snow cover appear as red, liquid water on the ground as black, liquid water clouds as white and ice clouds as peach. The blue arrows point north. Image courtesy of MODIS Rapid Response Project at NASA/GSFC: <http://rapidfire.sci.gsfc.nasa.gov>.

Title Page

Abstract

Introduction

Conclusions

References

Tables

Figures

I◀

▶I

◀

▶

Back

Close

Full Screen / Esc

Printer-friendly Version

Interactive Discussion



Aerosol distribution
around Svalbard

A. Dörnbrack et al.

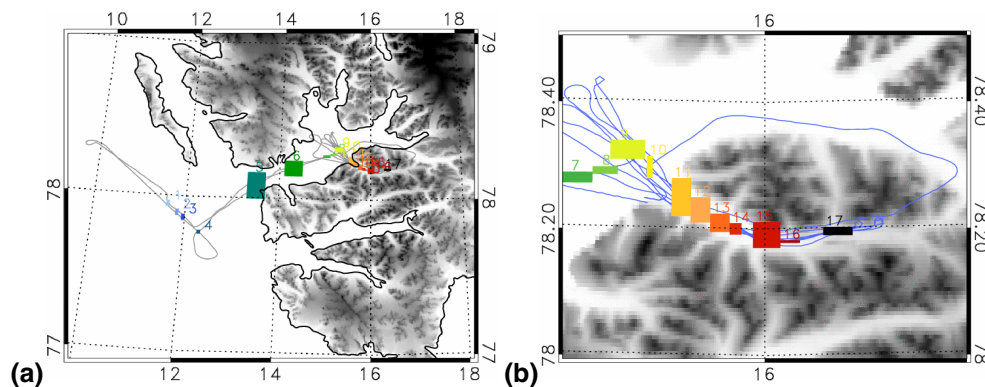


Fig. 3. Locations of the areas where vertical aerosol backscatter ratio ($R_{532\text{ nm}}$, dimensionless) and depolarization ($\delta_{532\text{ nm}}$, dimensionless) profiles were taken on 18 May 2004. As listed in Table 1, consecutive periods of the AMALi observations onboard the Polar 2 were used to calculate the averaged $R_{532\text{ nm}}$ and $\delta_{532\text{ nm}}$ profiles in the respective areas as shown in Figs. 4 and 5: The color code of a particular area refers to the color code of the associated profile.

[Title Page](#)[Abstract](#)[Introduction](#)[Conclusions](#)[References](#)[Tables](#)[Figures](#)[◀](#)[▶](#)[◀](#)[▶](#)[Back](#)[Close](#)[Full Screen / Esc](#)[Printer-friendly Version](#)[Interactive Discussion](#)

Aerosol distribution
around Svalbard

A. Dörnbrack et al.

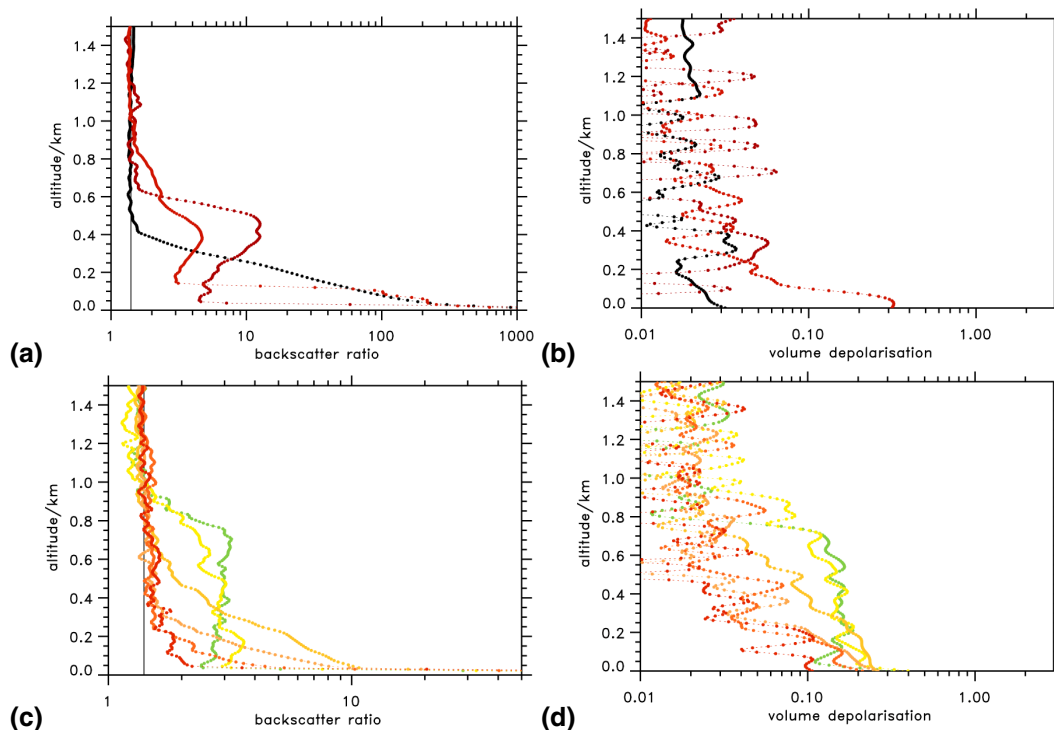


Fig. 4. Backscatter ratio (left column) and volume depolarisation (right column) at 532 nm inside the Adventdalen as measured along the Polar 2 flight path on 18 May 2004. **(a)** and **(b)** depict profiles calculated in areas No. 15 to 17 at the eastern part, **(c)** and **(d)** profiles calculated in areas No. 10 to 14 at the western part of the Adventdalen. Additionally, profile No. 8 (the green lines) is added to facilitate the visualisation of the dust plume evolution from the Adventdalen to its exit in the Isfjorden. The color coding refers to the respective segments of the flight path, see Fig. 3 and Table 1.

[Title Page](#)[Abstract](#)[Introduction](#)[Conclusions](#)[References](#)[Tables](#)[Figures](#)[◀](#)[▶](#)[◀](#)[▶](#)[Back](#)[Close](#)[Full Screen / Esc](#)[Printer-friendly Version](#)[Interactive Discussion](#)

Aerosol distribution
around Svalbard

A. Dörnbrack et al.

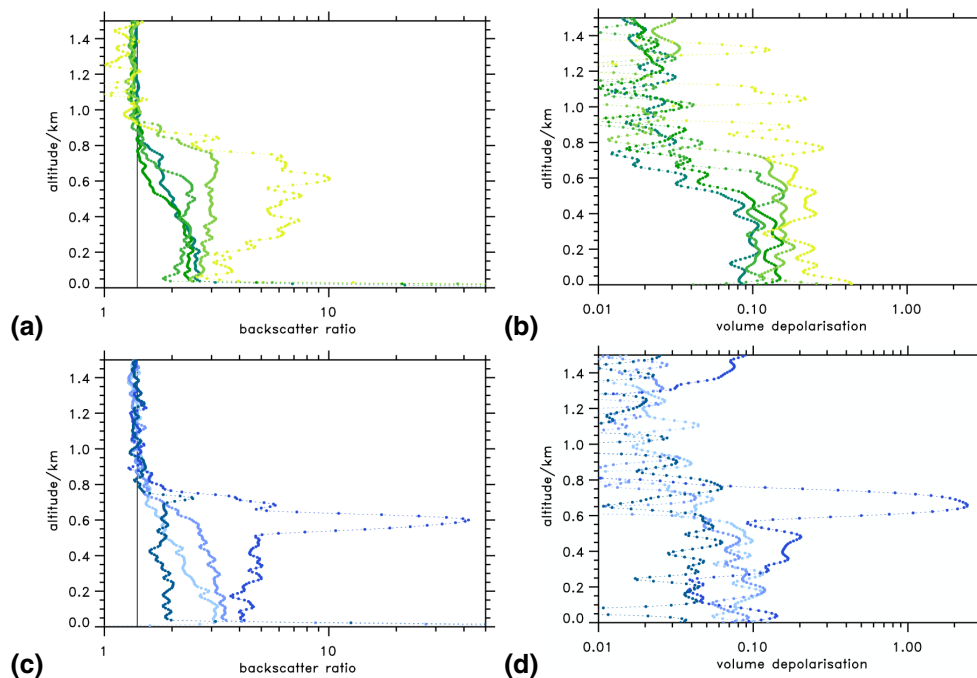


Fig. 5. Backscatter Ratio (left column) and volume depolarisation (right column) at 532 nm above open water as measured along the Polar 2 flight path on 18 May 2004. **(a)** and **(b)** depict profiles calculated in areas No. 5 to 9 above the Isfjorden, **(c)** and **(d)** profiles calculated in areas No.1 to 4 in the lee of Svalbard. The color coding refers to the respective segments of the flight path, see Fig. 3 and Table 1.

[Title Page](#)[Abstract](#)[Introduction](#)[Conclusions](#)[References](#)[Tables](#)[Figures](#)[◀](#)[▶](#)[◀](#)[▶](#)[Back](#)[Close](#)[Full Screen / Esc](#)[Printer-friendly Version](#)[Interactive Discussion](#)

Aerosol distribution
around Svalbard

A. Dörnbrack et al.

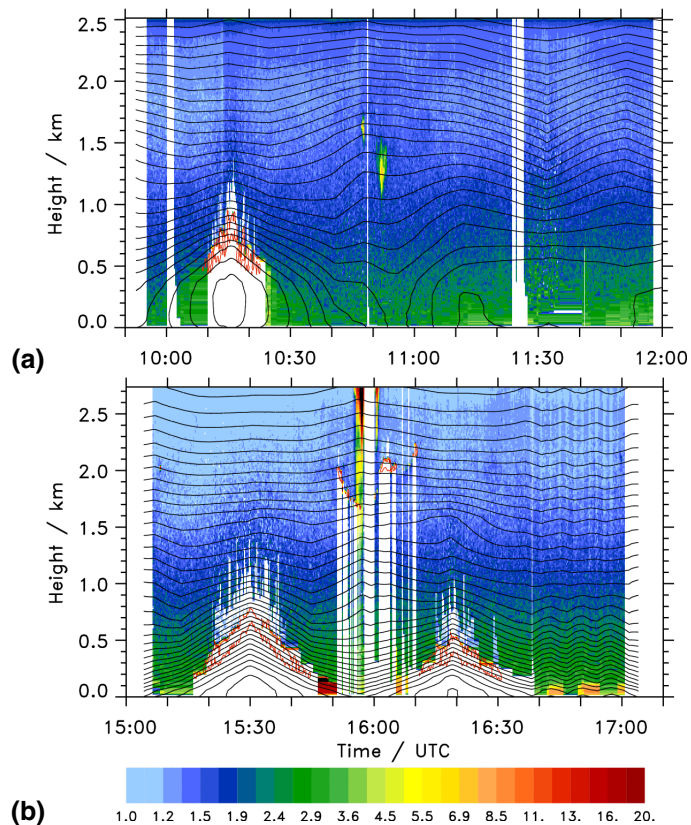


Fig. 6. Backscatter ratio $R_{532\text{nm}}$ (colour-shaded) and range corrected signal strength $S = P h^2 = 2$ and $4 \cdot 10^{-9}$ (red contour lines) along two flight tracks on 19 May 2004 **(a)** and on 21 May 2004 **(b)**, respectively. Black contour lines mark the potential temperature Θ with $\Delta\Theta = 0.5\text{ K}$ interpolated onto the flight paths (see Fig. 1). Meteorological data from operational T511/L60 ECMWF analyses.

Title Page

Abstract

Introduction

Conclusions

References

Tables

Figures

◀

▶

◀

▶

Back

Close

Full Screen / Esc

Printer-friendly Version

Interactive Discussion



Aerosol distribution
around Svalbard

A. Dörnbrack et al.

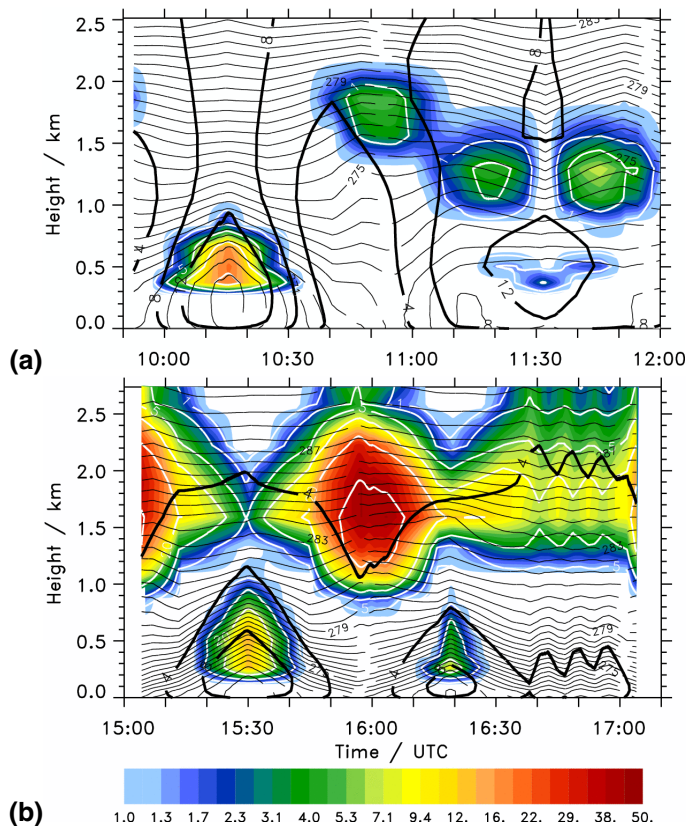


Fig. 7. Cloud liquid water content (mg/kg, colour-shaded), cloud ice water content (mg/kg, white contour lines), horizontal wind speed (ms⁻¹, thick black lines), and potential temperature Θ with $\Delta\Theta=0.5$ K interpolated onto the two flight tracks on 19 May 2004 (a) and on 21 May 2004 (b), respectively. Meteorological data from operational T511/L60 ECMWF analyses.

[Title Page](#)[Abstract](#)[Introduction](#)[Conclusions](#)[References](#)[Tables](#)[Figures](#)[◀](#)[▶](#)[◀](#)[▶](#)[Back](#)[Close](#)[Full Screen / Esc](#)[Printer-friendly Version](#)[Interactive Discussion](#)

Aerosol distribution
around Svalbard

A. Dörnbrack et al.

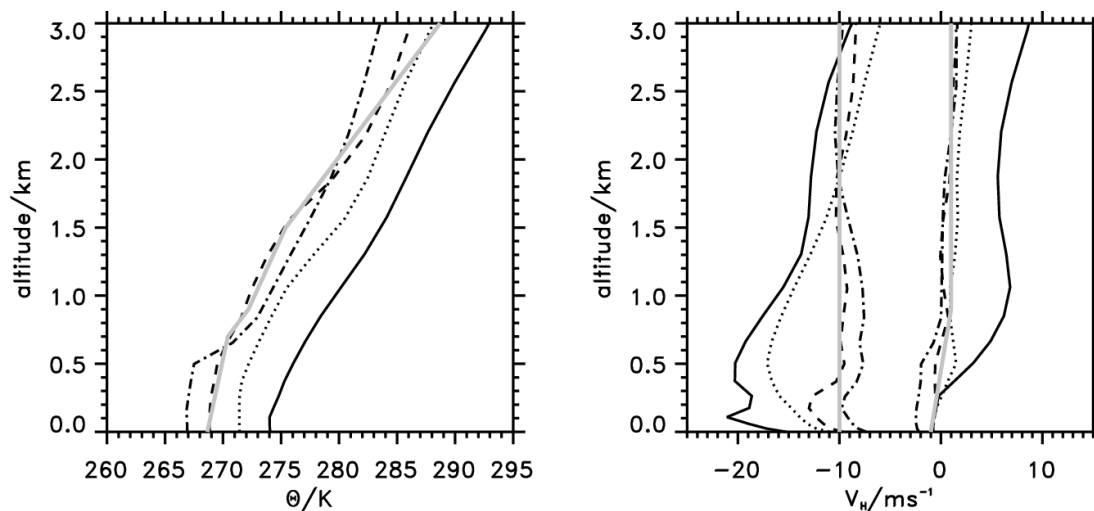


Fig. 8. Upstream profiles of potential temperature Θ (left panel) and the zonal (all profiles negative values) and meridional wind speed at 30° E and 75° N (solid line), 77° N (dotted line), 79° N (dashed line), and at 81° N (dash-dotted line) valida at 19 May 2004 12:00 UTC. Meteorological data are based on operational T511/L60 ECMWF analyses. The bold grey lines mark the initial conditions of the EULAG simulations.

[Title Page](#)[Abstract](#)[Introduction](#)[Conclusions](#)[References](#)[Tables](#)[Figures](#)[◀](#)[▶](#)[◀](#)[▶](#)[Back](#)[Close](#)[Full Screen / Esc](#)[Printer-friendly Version](#)[Interactive Discussion](#)

Aerosol distribution
around Svalbard

A. Dörnbrack et al.

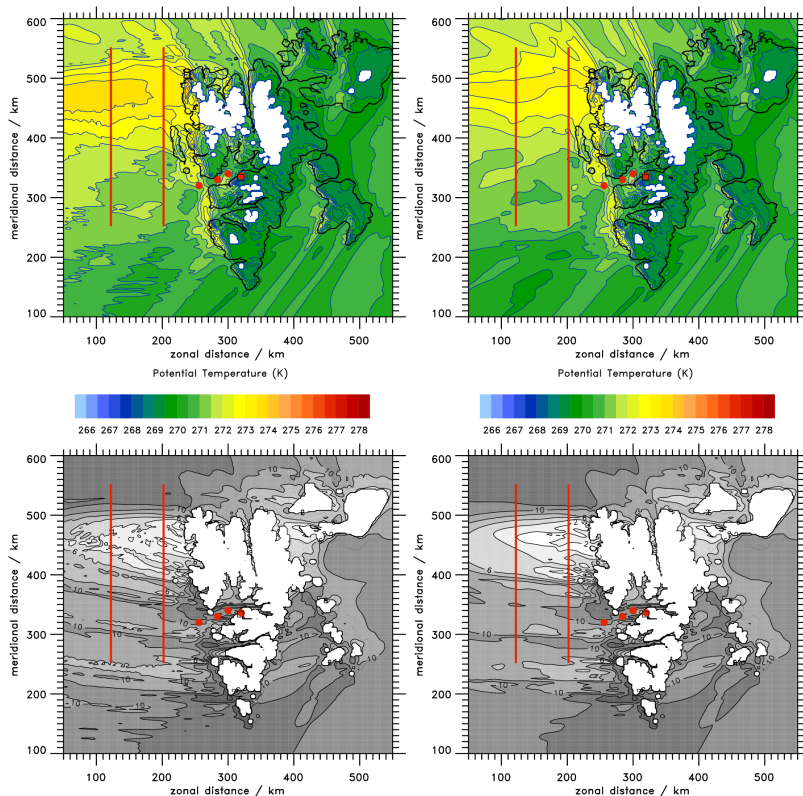


Fig. 9. Simulated potential temperature Θ (K, $\Delta\Theta=0.5$ K, upper row) at 800 m altitude and horizontal wind speed V_H (ms^{-1} , $\Delta V_H=2$ ms^{-1} , lower row) at 500 m altitude after 18 h simulation time. Left column: results from a run with surface heat flux; right column: results from a run without surface heat flux. The straight red lines mark the baseline of the vertical sections as shown in Fig. 11, and the red circles the locations of the vertical profiles as shown in Fig. 12.

[Title Page](#)[Abstract](#)[Introduction](#)[Conclusions](#)[References](#)[Tables](#)[Figures](#)[◀](#)[▶](#)[◀](#)[▶](#)[Back](#)[Close](#)[Full Screen / Esc](#)[Printer-friendly Version](#)[Interactive Discussion](#)

Aerosol distribution
around Svalbard

A. Dörnbrack et al.

Title Page

Abstract

Introduction

Conclusions

References

Tables

Figures

◀

▶

◀

▶

Back

Close

Full Screen / Esc

Printer-friendly Version

Interactive Discussion

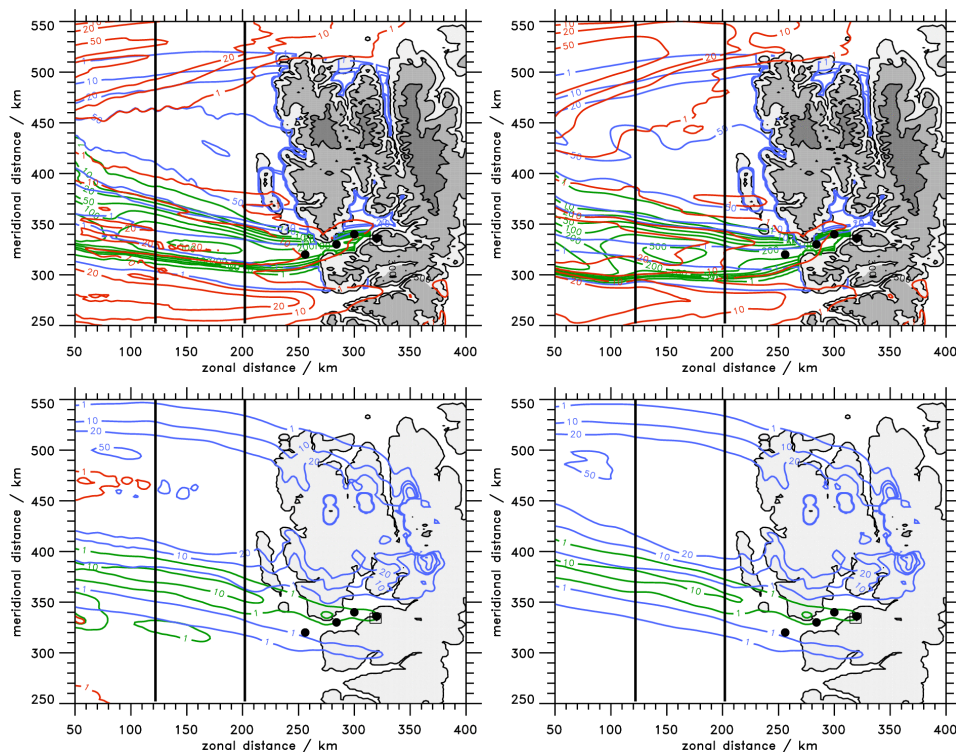


Fig. 10. Horizontal aerosol distribution at 300 m (top row) and 1200 m altitude (lower row) after 18 h simulation time. Left column: results from a run with surface heat flux; right column: results from a run without surface heat flux. The colors of the contour lines denote the different aerosol species: red – sea salt aerosol, green – dust, and blue snow and ice crystals. The straight black lines mark the baseline of the vertical sections as shown in Fig. 11, and the black circles mark the locations of the vertical profiles as shown in Fig. 12.

Aerosol distribution around Svalbard

A. Dörnbrack et al.

Title Page

Abstract

Introduction

Conclusions

References

Tables

Figures

◀

▶

◀

▶

Back

Close

Full Screen / Esc

Printer-friendly Version

Interactive Discussion

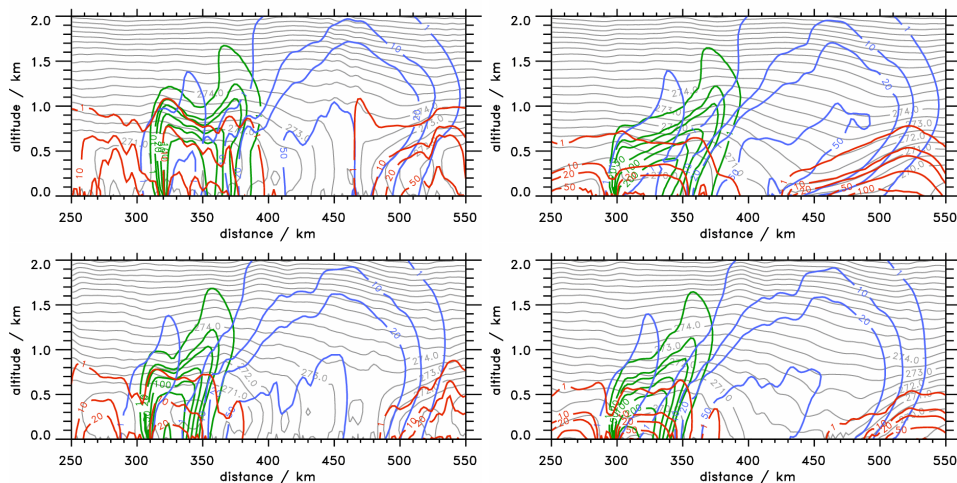


Fig. 11. Vertical aerosol distribution in the lee of Svalbard along the two baselines as shown in Figs. 9 and 10 at $x=122$ km (top row) and $x=202$ km (lower row) after 18 h simulation time. Left column: results from a run with surface heat flux; right column: results from a run without surface heat flux. The colors of the contour lines denote the different aerosol species: red – sea salt aerosol, green – dust, and blue snow and ice crystals. The black solid lines denote the potential temperature Θ (K, $\Delta\Theta=0.5$ K).

Aerosol distribution
around Svalbard

A. Dörnbrack et al.

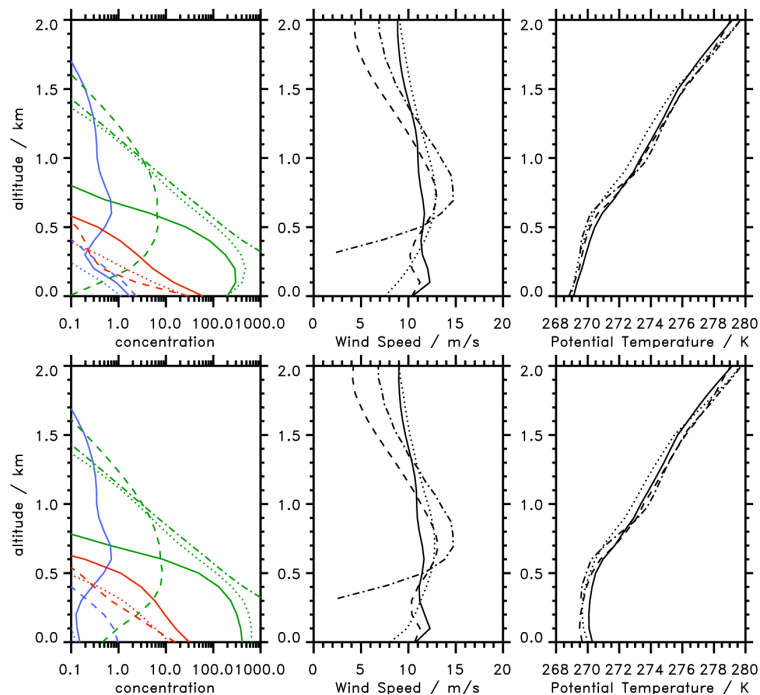


Fig. 12. Vertical profiles of the aerosol concentrations, the magnitude of the horizontal wind speed, and the potential temperature at the marked locations in Figs. 9 and 10 after 18 h simulation time. The four positions are labeled from west to east in the following order: solid, dotted, dashed, dash-dotted. The colors of the concentration lines denote the different aerosol species: red – sea salt aerosol, green – dust, and blue snow and ice crystals. Top row: results from a run without surface heat flux; bottom row: results from a run with surface heat flux.

[Title Page](#)[Abstract](#)[Introduction](#)[Conclusions](#)[References](#)[Tables](#)[Figures](#)[◀](#)[▶](#)[◀](#)[▶](#)[Back](#)[Close](#)[Full Screen / Esc](#)[Printer-friendly Version](#)[Interactive Discussion](#)